

# Development and Characterization of a Second Harmonic Generator and Mach-Zehnder Interferometer towards a Frequency-Dependent Squeezed Light Source

Nathaniel Morrison<sup>1</sup>

Mentored by: Pierre-François Cohadon<sup>2</sup> and Sheon Chua<sup>3</sup>

(Dated: July 31, 2019)

## I. INTRODUCTION

Since its first direct observation in 2015, gravitational wave astronomy has provided a powerful new tool for the study of astronomical objects and events [1]. Sensing of gravitational waves relies on the detection of very small-scale distortions in space-time. Currently, interferometers such as the modified Michelson-type systems in use at the LIGO and Virgo sites (see Fig 1) have provided the greatest sensitivity to such fluctuations, and are regularly detecting gravitational waves. Their sensitivity is limited by a variety of noise sources, including quantum noise, induced by fundamental fluctuations in the light fields used by interferometers to measure gravitational waves. Quantum noise cannot be entirely eliminated. However, optical squeezing, a phenomenon in which fluctuation in one degree of freedom of a light field is reduced at the cost of increasing fluctuation in another, provides a possible means of increasing sensitivity beyond the quantum limit. Squeezed light is already in use at both LIGO and Virgo. Further reduction in quantum noise, however, requires something more: frequency-dependent squeezed light. Such a system would dynamically change the degree of freedom in which fluctuation is minimized to optimize sensitivity across the entire frequency spectrum. The Optomechanics and Quantum Measurement team at Laboratoire Kastler Brossel (LKB), in collaboration with the the Laboratoire de l'Accélérateur Linéaire (LAL), the Laboratoire d'Annecy-le-Vieux de Physique des Particules (LAPP) and the Laboratoire des Matériaux Avancés (LMA), is seeking to demonstrate frequency-dependent squeezing in the frequency range of interest for gravitational wave detection, with the goal of implementing such a system at Virgo before the next science run. We describe the construction and characterization of a part of this system, including: an infrared laser to provide the light to be squeezed; a Second Harmonic Generator (SHG) to convert infrared laser light into green laser light to drive the Optical Parametric Oscillator (OPO), the component which induces squeezing; and a Mach-Zehnder Interferome-

ter (MZI) to stabilize the green light produced by the SHG.

## II. BACKGROUND

### A. Gravitational Wave Interferometry

At present, Fabry-Perot-Michelson-type interferometers are the most reliable and sensitive apparatus available for gravitational wave detection. A simplified optical diagram of such a system can be seen in Fig 1a. A laser is fired through a beamsplitter into two “arms”, the North arm and the East arm, at the ends of which are mirrors. Light in each arm is reflected back towards the beamsplitter, where the two fields mix before entering the “dark port” and measurement photodetector. The North and East arms’ lengths are kept equal, up to an integer multiple of the laser wavelength, so that light from each destructively interferes when passing into the dark port. This results in little to no light reaching the detector. A passing gravitational wave will shorten one of the arms while stretching the other, generating a phase difference between the light from each arm. The fields no longer exhibit total destructive interference upon entering the dark port, resulting in a signal being generated by the photodetector. As the gravitational wave continues to pass through the detector, the relative arm length will continue to oscillate, creating interference fringes on the detector. The magnitude and frequency of the signal the detector generates can then be analyzed to provide rich information about the event that produced the wave.

Also seen in Fig 1a are additional mirrors in the middle of each of the four branches of the interferometer. These mirrors form a series of optical cavities, optical elements consisting of two mirrors facing one another. When a light field enters an optical cavity, it reflects off each mirror multiple times before finally exiting the cavity, with the average number of reflections before transmission determined by the reflectivity of the mirrors. If the round-trip cavity length is an integer multiple of the wavelength of the field, the many reflected beams constructively interfere with each other, boosting total optical power in the cavity - a “resonant” state. This effect is used in the interferometer in a process called power recycling to achieve effective laser powers far greater than the input laser power. The mirror in front of the laser forms an optical cavity with the rest of the interferometer since, when the arm lengths are held such that no light enters the dark port, all light is reflected back towards the laser and the system acts

<sup>1</sup> Undergraduate, Department of Physics and Astronomy and Department of Statistics and Mathematics, California State University of Long Beach, Long Beach, CA 90840, USA

<sup>2</sup> Associate Professor, Laboratoire Kastler Brossel, Sorbonne Université, Paris 05, France

<sup>3</sup> Post-Doctoral Fellow, Laboratoire Kastler Brossel, Sorbonne Université, Paris 05, France

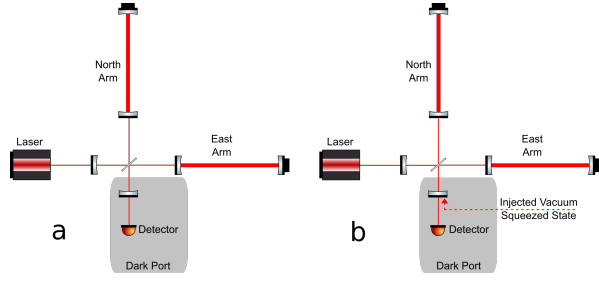


Fig. 1. Simplified optical diagrams of Fabry-Perot-Michelson interferometers similar to those in use at LIGO and Virgo. a) displays an interferometer without squeezed vacuum injection; the dark port contains a coherent vacuum state which will introduce a significant amount of noise to the light en route to the detector. b) displays an interferometer with frequency-independent squeezed vacuum injection; the squeezed vacuum state replaces the coherent vacuum state in the dark port. Setup b) is currently in use at both LIGO and Virgo.

like a single mirror. Laser power throughout the system is thus increased, with the added advantage of increased power stability. The cavities in the North and East arms, the features differentiating a Fabry-Perot-Michelson interferometer from a Michelson interferometer, further boost laser power and increase sensitivity to gravitational waves within a specific frequency range. Finally, the mirror in the dark port serves to boost the optical power of the signal light field, enhancing photodetector response [7].

### B. Noise in Interferometers

Limits on interferometer sensitivity are due to noise from various sources, including thermal noise from component coatings, seismic noise from the surrounding Earth, Newtonian noise from minute fluctuations in the local gravitational field, and quantum noise arising from the Heisenberg Uncertainty Principle in both the laser and the vacuum state near the system's photodetector. The amount of noise from each of these sources varies across the frequency spectrum; at present Newtonian and suspension thermal noise dominate at frequencies below 10-15 Hz and quantum noise - particularly quantum shot noise (QSN) - dominates at frequencies above about 110 Hz (see Fig 2). Once Virgo reaches its design sensitivity, as it is expected to after a series of planned upgrades, it will be limited by a different manifestation of quantum noise, quantum radiation pressure noise (QRPN), through much of the low-frequency spectrum [5]. The reduction of quantum noise is thus necessary to increase detector sensitivity.

Quantum noise arises from fundamental uncertainty in two parameters of a light field, amplitude and phase. The Hamiltonian of light can be represented as a superposition of quantum harmonic oscillator Hamiltonians which, when written in terms of the boson creation and annihilation operators  $\hat{a}_k^\dagger$  and  $\hat{a}_k$ , have the form [2]:

$$\hat{H} = \sum_k \hbar \omega_k (\hat{a}_k^\dagger \hat{a}_k + \frac{1}{2}) \quad (1)$$

Where  $\omega_k$  is the angular mode frequency. Utilizing this formalism, it is possible to construct closed-form formulae

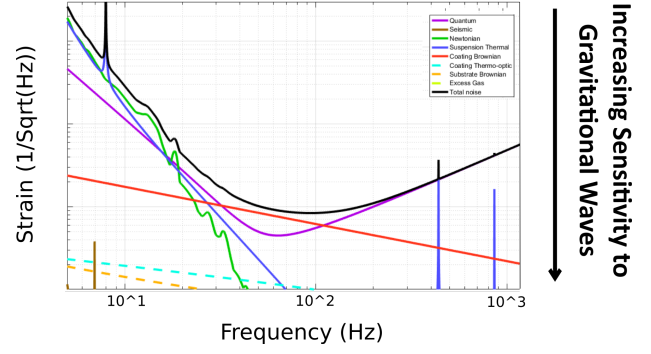


Fig. 2. Effect of noise from various sources on current Virgo sensitivity, given in strain-equivalent magnitude. Greater strain resolution is equivalent to greater sensitivity to gravitational waves; the "total noise" line represents the current absolute lower limit of strain resolution.

for two new Hermitian operators:

$$\hat{X}_1 = \hat{a}_k + \hat{a}_k^\dagger \quad (2)$$

$$\hat{X}_2 = i(\hat{a}_k - \hat{a}_k^\dagger) \quad (3)$$

$\hat{X}_1$  is the amplitude quadrature of the electromagnetic field, returning the amplitude of the field when applied to the field's wavefunction.  $\hat{X}_2$  is the phase quadrature, returning the phase of the field when applied to the field's wavefunction. These operators do not commute:

$$[\hat{X}_1, \hat{X}_2] = 2i \quad (4)$$

Therefore, they must obey a Heisenberg uncertainty relation:

$$\Delta \hat{X}_1 \Delta \hat{X}_2 \geq 1 \quad (5)$$

Where  $\Delta \hat{X}_1$  and  $\Delta \hat{X}_2$  are the variances in  $\hat{X}_1$  and  $\hat{X}_2$ , respectively. Thus, even with all other sources of noise removed from a system, there will still be error introduced by these fundamental fluctuations in amplitude and phase. This manifests as QRPN, induced by amplitude fluctuations affecting the movement of suspended mirrors and other optics, and QSN, induced by phase fluctuations hindering an interferometer's ability to resolve small phase differences in the field from each arm. These two noise sources are not evenly spread across the frequency spectrum, with QRPN dominating at low frequencies and QSN dominating at high frequencies; the Standard Quantum Limit (SQL) is defined as the frequency at which the average magnitude of the two types of noise are equal (see Fig 3).

### C. States of Light

To understand the effect of quantum noise on a light field, it is first necessary to understand the various states of light. Within a Fabry-Perot-Michelson interferometer, two states dominate: bright coherent states and vacuum states. A coherent state is a state in which uncertainty is minimized and equally distributed across both quadratures, e.g.  $\Delta \hat{X}_1 = 1$  and  $\Delta \hat{X}_2 = 1$ . A bright coherent state is a coherent state in which these fluctuations occur around a nonzero average amplitude. Such a state can be represented in amplitude-phase space by a vector as shown in Fig 4a. Note that rather

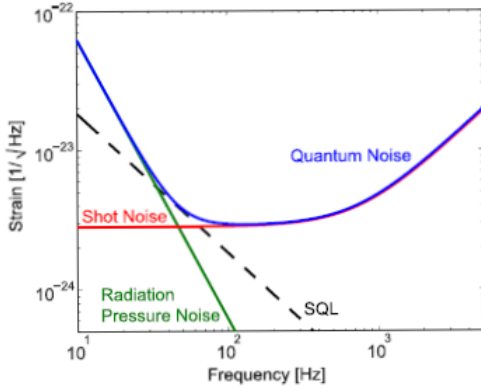


Fig. 3. Strain-equivalent noise level vs frequency in a Fabry-Perot-Michelson interferometer. QRPN is the primary noise source at frequencies below the SQL, while QSN dominates at frequencies above the SQL. The net effect of both sources is the overall “Quantum Noise”. Retrieved from Chua et al.[2]

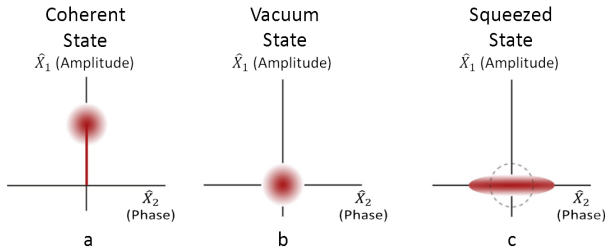


Fig. 4. Phasors representing various states of light. The red circle/ellipse at the end of the vector represents the range of possible locations of the actual phasor each time a measurement is made on an uncertain state, with the intensity of color indicating relative probability. a) is the phasor for a bright coherent state, b) for a coherent vacuum state, and c) for a squeezed vacuum state. Retrieved from Chua et al.[2]

than terminating at a single point, the vector instead ends in a “variance ball,” with the center point being the average amplitude and phase of the field and the opacity of coloration representing the relative likelihood that a measurement of the field will return the amplitude or phase at that point. Lasers used in modern gravitational wave detectors are well approximated as bright coherent states, and introduce the noise expected of such a state into the interferometer.

A vacuum state is the natural state of light present at all points in space where no other state exists. The uncertainty relation in Eq 5 applies even when no photons are present, generating minute fluctuations in amplitude and phase even in an otherwise dark environment. These fluctuations cannot be directly detected, but their effect can be seen in the noise they inject into other passing states of light. Vacuum states are naturally coherent states, with variance in amplitude and phase both exactly one and a mean amplitude and phase of zero, as shown by the amplitude-phase space vector in Fig 4b. Since most modern gravitational wave interferometer setups are operated at or near a dark fringe, very little laser light passes through to the dark port (see Fig 1), and likewise very little laser noise is encountered in measurements. Most noise instead comes from signal interaction with vacuum states.

Squeezed light is a third state, in which the variance in one quadrature is made to be greater than one so that the variance in the second quadrature may be less than one, e.g. if  $\Delta\hat{X}_1 = S > 1$ , then  $\Delta\hat{X}_2 = 1/S < 1$  still satisfies Eq 5. Both vacuum and bright states may be squeezed along any line in amplitude-phase space; see the example of an amplitude-squeezed vacuum state in Fig 4c. Note that the variance ball is now a “variance ellipse;” uncertainty in amplitude is reduced, at the cost of increasing uncertainty in phase [2].

#### D. Squeezed Light in Interferometers

Squeezed light provides a means of overcoming the quantum noise limit. Squeezing can be applied to both the laser and the vacuum states in an interferometer to improve response; phase-squeezed vacuum injection into the dark port (see Fig 1b) has already been implemented at both LIGO and Virgo to enhance sensitivity at high frequencies, where QSN is the limiting type of noise. The squeezed vacuum state replaces the natural coherent vacuum state in the dark port, lowering phase noise while increasing amplitude noise. The effect of various types of squeezing on the quantum noise limit can be seen in Fig 5. In each case of uniform squeezing across the bandwidth, sensitivity is enhanced in some frequency range and decreased elsewhere due to the frequency-dependence of the relative magnitude of QRPN and QSN. At LIGO and Virgo, this is not currently a problem as even with phase squeezing QRPN is not the limiting noise source at low frequencies (see Fig. 2). Once design sensitivity is reached, however, the sensitivity will be limited by QRPN in this regime. An ideal squeezer would thus be frequency dependent, providing amplitude squeezing at low frequencies where QRPN dominates, rotating the “variance ellipse” in amplitude-phase space through mid-range frequencies where the magnitudes of QRPN and QSN are comparable, and providing phase squeezing at high frequencies where QSN dominates. This would provide the uniform improvement seen in the “frequency-dependent squeezing” curve in Fig. 5.

#### E. The ExSqueeze Project: Towards a Frequency-Dependent Squeezer

The Experimental Squeezing for Optomechanics (ExSqueeze) project, led by LKB with support from LAL, LAPP and LMA, is a French Agence Nationale de la Recherche - funded program to develop and demonstrate a frequency-dependent squeezed vacuum light source in the frequency range of interest for gravitational wave detection, with a goal of at least 6 dB of squeezing across the audio band and a corner frequency - the frequency about which squeezing rotates from amplitude to phase - between 1 and 10 kHz [5]. Frequency-dependent squeezing has previously been demonstrated, but with a corner frequency in the megahertz range [8], far above the frequency of currently detectable gravitational waves. To achieve a corner frequency in the audio band, a rotation cavity is to be used.

A rotation cavity is an optical cavity, and is functionally

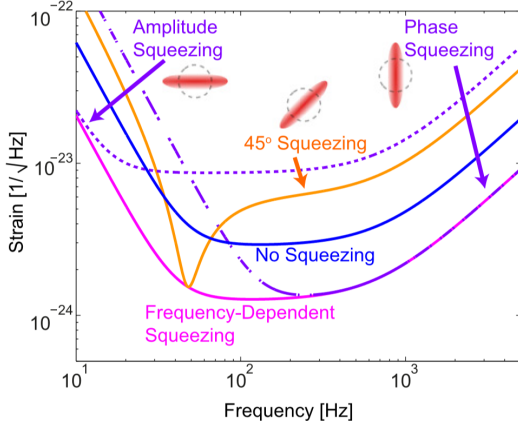


Fig. 5. Effect of various types of squeezing on the net quantum noise limit in gravitational wave detection. Lower values of detectable strain indicate greater sensitivity. Retrieved from Chua et al.[2]

identical to the optical cavities described in the preceding sections. As well as affecting the amplitude of incident light fields, cavities induce a phase shift about a particular corner frequency. The corner frequency will be at the half-maximum point near a cavity resonance peak. When a squeezed light field passes through a cavity, the phase shift will “rotate” the amplitude-phase space ellipse in Fig 4c. The degree of rotation depends on the difference between the field and corner frequencies; fields near cavity resonance will experience no rotation, fields at the corner frequency will experience a  $45^\circ$  rotation, and fields far from cavity resonance will experience a  $90^\circ$  rotation.

The corner frequency is determined by the finesse and length of the rotation cavity.

$$f_c = f_{HWHM} = \frac{c}{4LF} \quad (6)$$

Where  $c$  is the speed of light,  $L$  is the length of the cavity, and the finesse  $F$  is given by [7]:

$$F = \frac{\pi}{2\arcsin(\frac{1-r_1r_2}{2\sqrt{r_1r_2}})} \quad (7)$$

Where  $r_1$  and  $r_2$  are the reflectivities of the two end mirrors. Achieving rotation in the audio band thus requires a cavity with ultra-low-loss optics to maximize finesse and great length. The 50 m long Cavit  s pour le Lock de Virgo Avanc   (CALVA) constructed by LAL, coupled with optical coatings fabricated by LMA, fulfills these requirements [5].

The squeezer and rotation cavity will be integrated at CALVA in the setup shown in Fig 6. Infrared laser light is converted to green laser light through a second harmonic generator and stabilized with a Mach-Zehnder Interferometer; the construction and characterization of these elements is described in this paper. The green light from this system is sent into a vacuum chamber, used to reduce acoustic noise and dust accumulation on optical components, and into an optical parametric oscillator. The OPO produces squeezed light, which is then sent to the rotation cavity before being reflected back and measured with a homodyne detector.

## F. Experimental Setup

In this paper we discuss the construction and characterization of the yellow-highlighted region in Fig 6. Fig 7 shows the final optical diagram for this part of the larger ExSqueez system at CALVA. A 2 W, 1064 nm Coherent Mephisto-2000NE laser is focused through a 200 mm focal length plano-convex lens and sent towards a half-wave plate and a quarter-wave plate to ensure the polarization axis is perpendicular to the benchtop. The beam is then passed through a Faraday isolator to prevent back-reflection into the laser before hitting another half-wave plate followed by a polarized beamsplitter. This permits fine adjustments of laser input power; as the waveplate is rotated such that the beam’s axis of polarization deviates from the vertical, more power is transmitted by the beamsplitter and less is reflected into the beam dump. The transmitted beam is then sent through another half-wave/quarter-wave plate pair to ensure perpendicular polarization before passing through a New Focus 4003 Electro-Optical Modulator (EOM) driven by a 12 MHz sine wave to induce frequency sidebands in the laser beam to be used in a Pound-Drever-Hall (PDH) control scheme. The modulated beam is then focused through a 75 mm focal length plano-convex lens into the SHG optical cavity, containing an MSHG1064-1.0 MgO:PPLN SHG crystal inside a PV10 oven controlled by an OC2 Temperature Controller, all from Covesion Ltd. The rear cavity mirror is attached to a PZT piezoelectric motor to allow for fine adjustments of cavity length. The transmitted infrared light is then passed through a 50 mm focal length plano-convex lens and an ND2 filter before terminating at a ThorLabs PDA10CF-EC photodetector (Detector A). Green light produced in the cavity is sent through a Faraday isolator to a Mach-Zehnder Interferometer. Another photodetector, a ThorLabs S1300 Power Meter (Detector C) was placed in the shown position only for conversion efficiency measurements. One output of the interferometer is sent to a beam dump (the “dump output”) while the other is passed through a second half-wave plate/polarized beamsplitter system to permit power control. Part of this beam is reflected through a 50 mm focal length plano-convex lens and into a Thor Labs PDA 10A2 photodetector (Detector B) by a 1% beam sampler, while the rest is sent through a half-wave/quarter-wave plate pair and transmitted to the In-Vacuum Bench as seen in Fig 6 (the “Green Output to In-Vacuum Bench”). Fig 8, 9 and 10 display the implementation of this setup at CALVA. The pictures are connected based on the labels at the ends of the optical paths, e.g. “A In” connects to “A Out,” etc.

## III. SECOND HARMONIC GENERATOR

The SHG consists of the optical cavity and SHG crystal within the shaded region marked “SHG Cavity” in Fig 7. The laser outputs infrared (IR) light at 1064 nm, but the OPO used to induce squeezing must be driven by a green (532 nm) laser beam. The SHG performs the frequency-doubling up-conversion of the laser beam from IR to green.



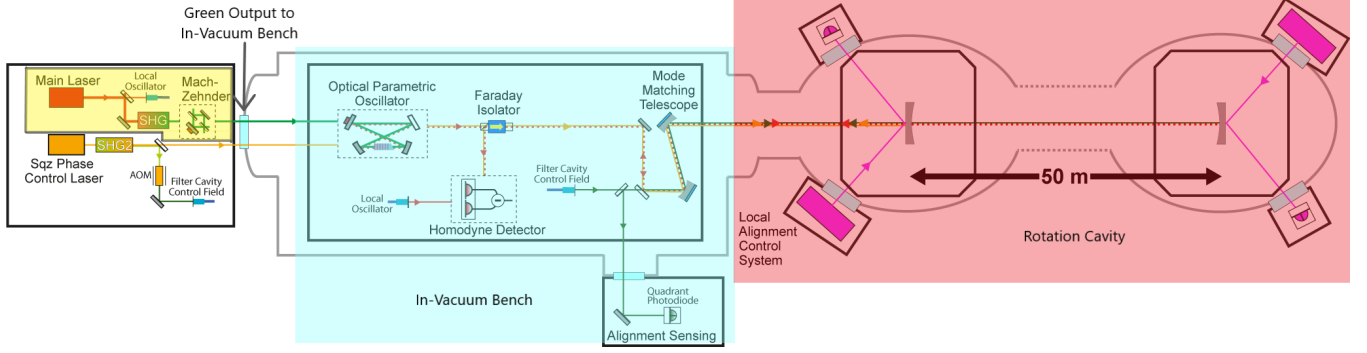


Fig. 6. Simplified optical diagram of planned ExSqueeze setup at CALVA. Highlighted in red is the rotation cavity, highlighted in blue is the In-Vacuum Bench, and highlighted in yellow is the part of the setup discussed in this paper.

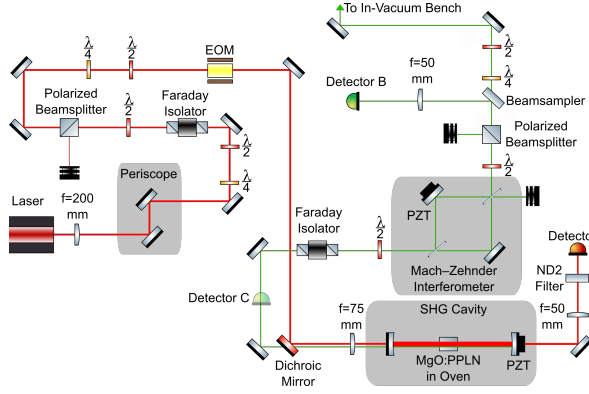


Fig. 7. Diagram of the optical setup constructed during this experiment. This setup is the yellow-highlighted section of the larger ExSqueeze frequency-dependent squeezer setup seen in Fig 6.

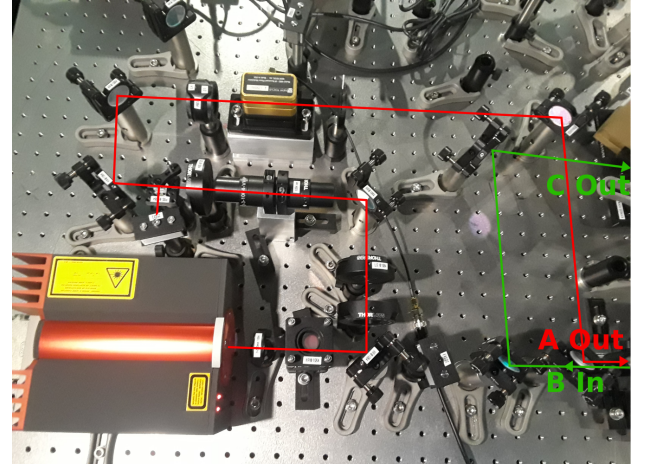


Fig. 8. Optical table at CALVA. In the picture is the laser and the entire optical path up to the SHG cavity focusing lens.

### A. Second Harmonic Generator Theory of Operation

A MgO doped PPLN birefringent crystal is pumped with a 1064 nm laser. Three wave mixing occurs within the crystal, a process in which two low energy 1064 nm photons are combined to create a single high energy 532 nm photon. As the input infrared field propagates further through the crystal, more photons are up-converted, increasing the output power. Without intervention, however, the input infrared field and the generated green light fields will eventually become out of phase, and interfere destructively. This results in a reversal of the nonlinear process, with the green photons down-converting to infrared photons. As the field continues to propagate, the conversion process will reverse again and output power will climb, resulting in a periodic fluctuation in output with propagation distance, as shown by the oscillating curve in Fig 11. The distance between extrema and zeros on the output plot is called the coherence length of the crystal.

This effect can be harnessed to boost output efficiency by periodically inverting the orientation of one axis of the crystal, termed "periodic polling". Inverting the axis inverts the conversion direction, and if the period of axis inversion is equal to an integer multiple of the coherence length, the increasing output shown in Fig 11 can be obtained. This technique produces quasi-phase matching between input and

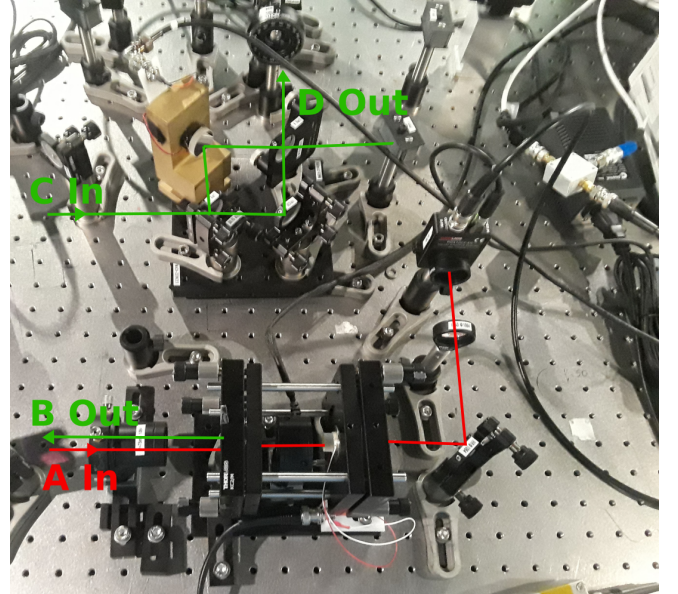


Fig. 9. Optical table at CALVA. In the picture are the SHG cavity and MZI. Note that the Faraday isolator preceding the MZI is not shown in this image.

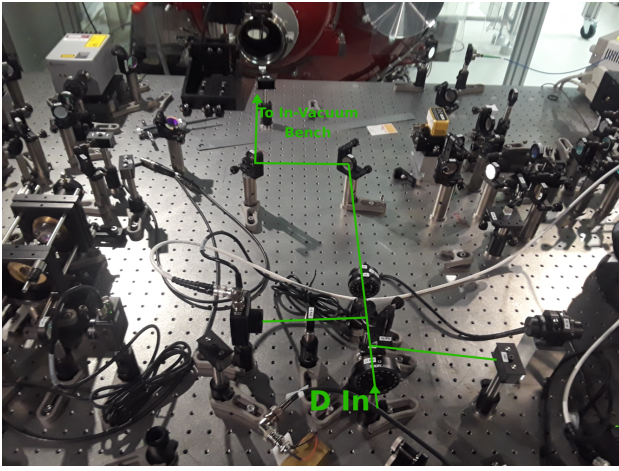


Fig. 10. Optical table at CALVA. In the picture is the optical path after the MZI.

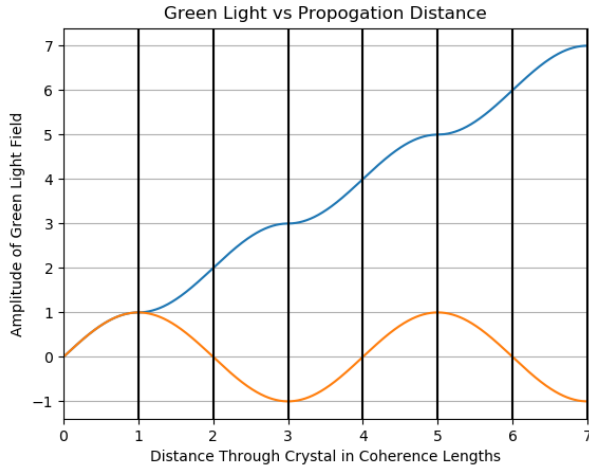


Fig. 11. Plot of green light produced by an infrared pump beam traveling through a non-periodically polled nonlinear crystal (orange plot, oscillating about zero amplitude) and a quasi-phase matched crystal (blue plot, increasing in amplitude).

generated fields, greatly enhancing the yield of the second harmonic generator [3][4]. However, because quasi-phase matching relies on precise distances between axis inversion sites, optimal conversion efficiency can only be reached and maintained if the crystal is kept at a specific temperature, as fluctuations in temperature result in expansion and contraction of the crystal. The crystal must therefore be kept in a carefully controlled oven to manage heating and cooling.

The optical cavity is used to further increase IR-to-green conversion efficiency by boosting effective pump power within the cavity. In the experimental setup, green light ultimately leaves the cavity by the leftmost mirror in Fig 7.

### B. SHG Temperature Sweep

As discussed in Section III-A, the temperature of an SHG crystal must be rigorously controlled to ensure proper phase matching and maximize conversion efficiency. To do this, the

temperature response of the crystal must be determined. A 1064 nm Innolight Mephisto 1000NE laser was fired through the crystal (outside of an optical cavity) as its temperature was varied, and the resulting green light was measured.

The crystal contains five periodically polled channels, each optimized for 1064 nm to 532 nm conversion at different crystal temperatures. The oven was heated to 50°C for initial alignment, the temperature suggested by the data sheet to be optimal for one of the periodically polled channels. The lateral position of the oven was then adjusted until both infrared and green light transmitted by the crystal were observed to be at a maximum, indicating that the beam was passing through the correct channel. Two dichroic mirrors were then placed between the output and a ThorLabs S1300 Power Meter. These mirrors transmit infrared but reflect green, and were used to filter out excess 1064 nm light. The power meter was set to further filter light of wavelengths other than 532 nm. A 150 mm focal length biconvex lens was also placed between the dichroic mirrors to focus the beam onto the power meter.

In order to operate the temperature controller, a Python program was written by the author to remotely set the desired temperature, enable and disable controller output, and change feedback loop parameters. Covision provides a proprietary application and a National Instruments LabVIEW API for interface with the device. However, as this controller will be used at both CALVA and the Virgo site, it is necessary to be able to interface with the controller through Python, a chosen language for Virgo software. The control program thus had to be reverse-engineered from the provided LabVIEW modules. See the Appendix for an excerpt from this program.

A temperature sweep of the SHG crystal was then performed. The crystal was slowly heated from 40°C to 60°C. At intervals, the power of green light produced by the crystal was measured. IR pump power was not measured, as only the relative magnitude of green output at different temperatures was needed. The output power is known to be a function of temperature such that

$$P(T) = A(\text{Sinc}(B(T - C)))^2 + D \quad (8)$$

Where  $T$  is the temperature, and  $A$ ,  $B$ ,  $C$ , and  $D$  are free parameters which depend upon laser and crystal properties. The  $\text{sinc}(x)$  function is defined to be

$$\begin{cases} \frac{\sin(x)}{x} & x \neq 0 \\ 1 & x = 0 \end{cases}$$

A Python program written by the author was used to approximate the parameters  $A$ ,  $B$ ,  $C$ , and  $D$  via least squares regression, and used to determine the temperature of peak efficiency and the full width at half maximum of the primary peak. The gathered data is shown in Fig 12, along with the interpolated fit function

$$P(T) = 87.99(\text{Sinc}(0.3082(T - 15.59)))^2 + 3.129 \quad (9)$$

The fit appears to match the data well along the central peak, although there appears to be a small offset between the fit

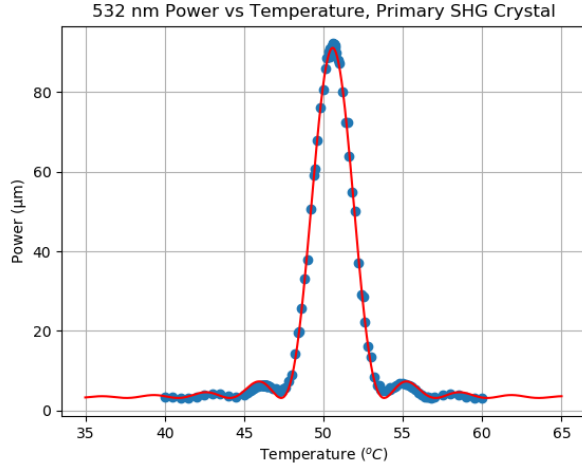


Fig. 12. Plot of green light produced by the SHG crystal vs crystal temperature. The blue points are measured values, and the red line is an interpolated sinc function fit.

and the measured powers in the side peaks. The offset is, however, minor. The fitted peak occurs at  $50.58^{\circ}\text{C}$ , and the full width at half maximum of the primary peak is  $2.94^{\circ}\text{C}$

### C. Laser Mode Matching

The laser has a Gaussian profile, narrowing to a minimum diameter at the beam “waist” and expanding to either side of this location. In order to maximize conversion efficiency in the SHG cavity, the axis of the beam should be aligned with the central axis of both the cavity and crystal, and the waist location should be at or near the center of the crystal.

1) *Coarse Alignment:* Waist location is in large part determined by the lens immediately preceding the cavity in Fig 7. To determine the ideal focal length and position of this lens, the shape of the input beam first had to be determined. A Thorlabs BP209-VIS/M Beam Profiler was used to measure power distribution across the beam wavefront, and thereby determine beam diameter, at multiple distances from an arbitrary reference point. This data was fed into a Python program written by the author which generates a best-fit Gaussian model and extrapolates waist size and location. The resulting fit can be seen in Fig 13. The program found a waist size of 0.184 mm approximately 270 mm behind the output of the laser head.

In order to ensure all of the input beam is incident on the SHG crystal, the input beam must be focused to a  $\leq 20\mu\text{m}$  waist size, with the location of this waist at the center of the crystal. A Python program written by the author was used to compute optimal lens placement to produce a waist of this size for a given focal length (see the Appendix for an excerpt from this program). The program was first used to compute the waist size and location following the 200 mm lens seen in Fig 7. This was found to be 0.295 mm at a location 400 mm from the  $f = 200$  mm lens. These parameters were then used to compute the ideal focal length and position of the pre-cavity focusing lens. The 75 mm focal length lens seen

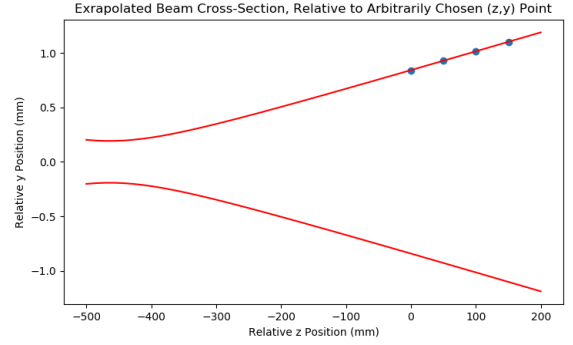


Fig. 13. Cross-section of the pump laser beam without additional optics. The origin point was chosen arbitrarily.

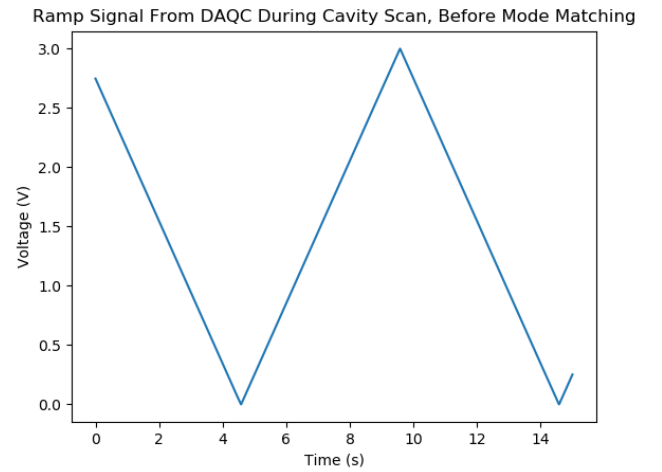


Fig. 14. Ramp signal sent to PZT during a cavity scan.

in Fig 7 was eventually chosen, producing the desired waist size of approximately 0.020 mm in the center of the cavity.

The two mirrors preceding the cavity, as well as the cavity mirrors themselves, were then adjusted to provide initial alignment of the cavity. Their position and angle were changed until green light was produced and IR light was observed to be exiting the cavity with a relatively circular beamfront.

2) *Fine Alignment:* Fine modal and alignment adjustments are made by “scanning” the cavity and observing its Free Spectral Range (FSR). “Scanning” refers to the introduction of a periodic oscillation in the PZT attached to one of the cavity mirrors. As the mirror is moved backwards and forwards, the length of the cavity changes, bringing the system into and out of resonance. Detector A in Fig 7 is used to measure the amount of infrared light transmitted by the cavity; when the mirror position is such that the cavity is out of resonance, the signal will be at a minimum. When the cavity is in resonance, the signal will be at a maximum. This signal, when viewed as a function of time, gives an FSR plot of the cavity.

The PZT inside the cavity was driven with a 0.1 Hz, 3



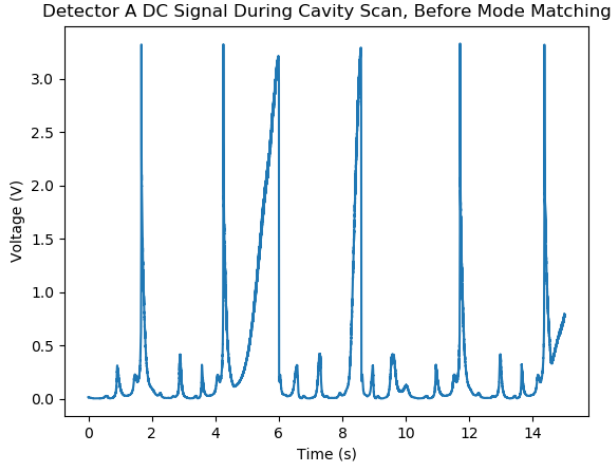


Fig. 15. DC signal from Detector A with PZT being driven by the ramp signal seen in Fig 14. The malformation of the peak starting at 5 seconds is due to the reversal of PZT direction around this time.

$V_{pp}$  symmetric triangle wave with a +1.5V offset from an Agilent 33220A function generator, passed through a Tegam 2350 High Voltage Amplifier set to 50x amplification. The signal from Detector A was viewed on a Tektronix TDS 1002 Oscilloscope. The ramp signal can be seen in Fig 14 and the corresponding signal from Detector A can be seen in Fig 15. Each peak in the FSR is a Gaussian mode. The tallest peaks are TEM00 modes. Only light in this mode is useful for squeezing once up-converted. An FSR begins at one of these peaks, and ends where the next appears; for example, the period from about 1.8 seconds to 4 seconds is one FSR. The very small peak immediately following the TEM00 peak, for example at about 2.2 seconds, is the TEM01 mode. This mode corresponds to the degree of misalignment of the beam and cavity axes; the greater the misalignment, the more power will be stored in the TEM01 mode relative to the TEM00 mode. Fine adjustments to alignment were thus made by attempting to minimize this peak. The peaks after the TEM01 peaks, for example at about 3 seconds, are the TEM02 modes of the laser beam. These modes correspond to the degree of mode mismatch between the input beam waist and the cavity's center. The waist was thus centered on the SHG crystal by adjusting both lens and cavity mirror position until this mode was minimized. Higher order modes also exist, for example the prominent TEM03 mode at about 3.5 seconds, but are not as significant as they can generally be minimized through minimization of the TEM01 and TEM02 modes.

Mode matching was first performed on the SHG cavity without the crystal present. Afterwards, the SHG crystal and oven were inserted into the middle of the cavity. Since the index of refraction of the crystal is greater than that of air, this effectively increased the length of the optical path within the cavity and generated greater TEM01 and TEM02 modes. These modes were minimized by the process described above. Once this was done, mode matching of the cavity

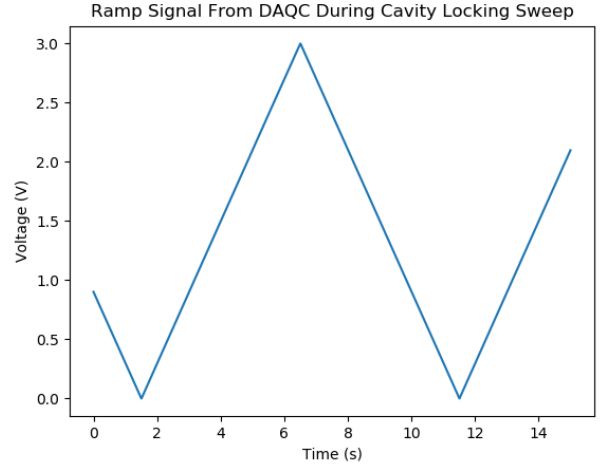


Fig. 16. Signal sent by DAQC to Cavity PZT during locking sweep.

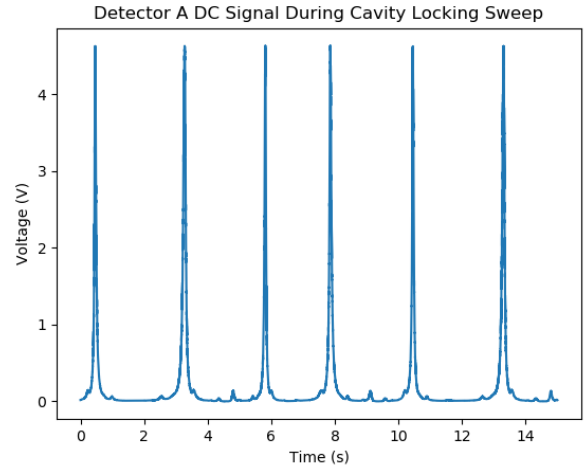


Fig. 17. DC signal from Detector A with PZT being driven by the ramp signal seen in Fig 16. The tall peaks are TEM00 modes; the very small peak immediately to the right of each TEM00 peak is the TEM01 mode, and the slightly taller peak after this is the TEM02 mode.

was complete. Due to imperfections in the components and vibrations in the optical bench, however, alignment gradually “drifts” over time. Because of this, the alignment process had to be repeated on a regular basis to ensure power remained primarily within the TEM00 mode. The post-matching FSR scan can be seen in Fig 17. Note the great reduction in size of the TEM01 and TEM02 modes relative to the TEM00 mode.

#### D. SHG Cavity Locking

To maximize conversion efficiency, the SHG cavity must be kept at resonance, its length held at an integer multiple of the laser wavelength - a “lock”. However, the cavity rests in a noisy environment, subject to seismic and acoustic vibrations in the air and optical bench as well as small fluctuations in the IR pump laser’s phase. The length of the cavity must therefore be constantly altered to correct for noise, and the

Pound-Drever-Hall (PDH) control scheme provides an ideal method of managing such a feedback loop.

1) *Pound-Drever-Hall Theory*: As seen in Fig 17, the response of the SHG cavity to changes in length is symmetric about resonance. Using the direct response of Detector A as the error signal for a control loop would indicate how far from resonance the system has drifted, but not the direction of the drift. The Pound-Drever-Hall technique provides a way to extract an error signal that is antisymmetric about resonance, allowing the control loop to determine both the magnitude and direction of needed corrections. Suppose an input monochromatic light field of frequency  $\omega$  is passed through an Electro-Optical Modulator (EOM), which modulates the phase of the field and induces frequencies sidebands at  $\omega - \omega_{mod}$  and  $\omega + \omega_{mod}$ , respectively, alongside the main carrier frequency. If the carrier (input monochromatic) light field is given by [6]:

$$E_c = E_0 e^{i\omega t} \quad (10)$$

Then the modulated field is given by

$$E_m = E_0 e^{i\omega t} - E_s e^{i(\omega - \omega_{mod})t} + E_s e^{i(\omega + \omega_{mod})t} \quad (11)$$

Where  $E_s$  is the amplitude of the sidebands. The mixed-frequency field is then passed into the cavity to be controlled. A cavity of length  $L$  consisting of two mirrors of reflectivity  $r$  and transmittivity  $t$  will act like a single mirror with a frequency-dependent reflectivity coefficient given by:

$$R(\omega) = \frac{r(e^{2Li\omega/c} - 1)}{1 - r^2 e^{2Li\omega/c}} \quad (12)$$

where  $c$  is the speed of light. When the frequency-modulated light field is incident upon the cavity, part of each frequency component is reflected from the cavity. The reflected light field is then the input light field scaled by the reflection coefficient:

$$E_r = E_0 R(\omega) e^{i\omega t} - E_s R(\omega - \omega_{mod}) e^{i(\omega - \omega_{mod})t} + E_s R(\omega + \omega_{mod}) e^{i(\omega + \omega_{mod})t} \quad (13)$$

A photodetector is placed in the path of the reflected beam, measuring its power:

$$\begin{aligned} P_r = |E_r|^2 = & P_c |R(\omega)|^2 + P_s (|R(\omega - \omega_{mod})|^2 \\ & + |R(\omega + \omega_{mod})|^2) \\ & + 2\sqrt{P_s P_c} \text{Re}\{R(\omega) R^*(\omega + \omega_{mod}) \\ & - R^*(\omega) R(\omega - \omega_{mod})\} \cos(\omega_{mod} t) \\ & + \text{Im}\{R(\omega) R^*(\omega + \omega_{mod}) \\ & - R^*(\omega) R(\omega - \omega_{mod})\} \sin(\omega_{mod} t) + \dots \end{aligned} \quad (14)$$

Where  $P_c$  is the power of the carrier signal and  $P_s$  is the power in each sideband. The first two terms are DC signals from the carrier and the two sidebands, respectively. The next term, a sum of a sine and cosine oscillating at the modulation frequency, derives from the beat signal generated when the sidebands interfere with the carrier. This term will provide the error signal, as it provides information on the phase of

the carrier. To isolate this term, the photodetector signal is mixed with the signal driving the EOM. A phase offset is induced in the mixer so that either the sine or cosine terms in the beat signal vanish. Without loss of generality, let it be the cosine term that vanishes, producing:

$$\begin{aligned} P_r \approx & P_c |R(\omega)|^2 + P_s (|R(\omega - \omega_{mod})|^2 \\ & + |R(\omega + \omega_{mod})|^2) \\ & + 2\sqrt{P_s P_c} \text{Im}\{R(\omega) R^*(\omega + \omega_{mod}) \\ & - R^*(\omega) R(\omega - \omega_{mod})\} \sin(\omega_{mod} t) + \dots \end{aligned} \quad (15)$$

The mixer will multiply each term in the photodetector signal by the EOM drive signal,  $\sin(\omega_{mod})$ . By the product-to-sum formula for the sine function, this will result in an output of:

$$\begin{aligned} P_{demod} \approx & P_c |R(\omega)|^2 \sin(\omega_{mod}) \\ & + P_s (|R(\omega - \omega_{mod})|^2 \\ & + |R(\omega + \omega_{mod})|^2) \sin(\omega_{mod}) \\ & + \sqrt{P_s P_c} \text{Im}\{R(\omega) R^*(\omega + \omega_{mod}) \\ & - R^*(\omega) R(\omega - \omega_{mod})\} (\cos((\omega_{mod} - \omega_{mod})t) \\ & - \cos((\omega_{mod} + \omega_{mod})t)) + \dots \end{aligned} \quad (16)$$

Note that now the first two terms are oscillating at the EOM frequency and the third term now consists of one part oscillating at  $\cos((2\omega_{mod})t)$  and one part that is a DC signal (since  $\cos((\omega_{mod} - \omega_{mod})t) = 1$ ). This signal may then be passed through a low-pass filter to remove the oscillating terms, leaving only the DC signal:

$$\epsilon = \sqrt{P_s P_c} \text{Im}\{R(\omega) R^*(\omega + \omega_{mod}) - R^*(\omega) R(\omega - \omega_{mod})\} \quad (17)$$

This is the error signal. Without loss of generality, let cavity reflectivity tend to zero at resonance. Then, an additional approximation may be made:

$$\epsilon \approx -\frac{4}{\pi} \sqrt{P_s P_c} \frac{2LF\delta\omega}{c} \quad (18)$$

Where  $\delta\omega$  is the difference between the laser frequency and cavity resonance. This approximation is only valid near resonance, but it is linear and therefore antisymmetric. This allows for the use of standard control loops which gradually adjust cavity length  $L$  until the error goes to zero and the cavity is locked.

Note that while this description utilizes the reflected field for control, the same principles apply to the system in use at CALVA, where the transmitted field is used instead.

2) *PDH Implementation*: To lock the SHG cavity, it must first be aligned and mode-matched as described in Section III-C. Once that is done, Detector A, the cavity PZT, and the EOM seen in Fig 7 are connected to a combined Data Acquisition and Control Board (hereafter referred to as the "DAQC") fabricated by LAPP. Fig 18 displays the layout of the electrical systems used. The circuit in Fig 18a gathers input from Detector A. A Mini-Circuits ZFBT-4R26W+ RF/DC splitter separates the DC and RF parts of the detector



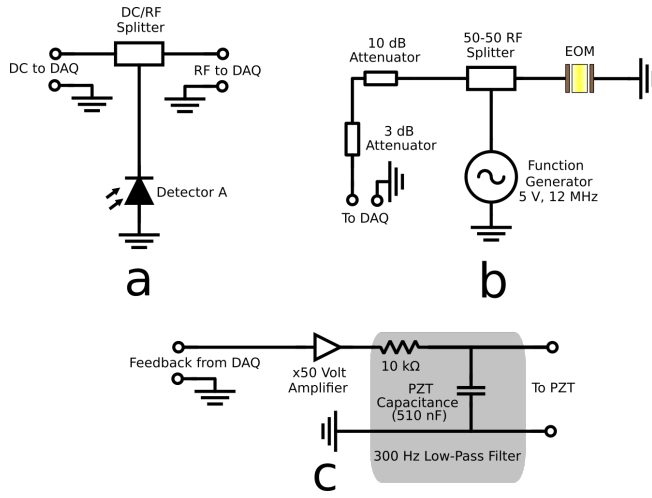


Fig. 18. Layout of electrical systems used to implement PDH locking of the SHG cavity seen in Fig 7.

signal and sends each to a different DAQC port. The DC signal is used for phase 1 of the locking process, while the RF signal is used for phase 2. The circuit in Fig 18b drives the EOM and provides the demodulation signal for the mixer. A 5  $V_{PP}$ , 12 MHz sine wave is delivered by an Agilent 33220A Function Generator to a Mini-Circuits ZFSCJ-2-2-S 50/50 RF splitter, which sends half of the signal through a pair of attenuators (to avoid electronic saturation) towards the mixer in the DAQC, and half into the EOM. The circuit in Fig 18c delivers the feedback signal from the DAQC to the PZT. The DAQC signal is passed through a Tegam 2350 High Voltage Amplifier set to x50 amplification and then through a 300 Hz low-pass filter formed by a resistor and the PZT's natural capacitance before reaching the PZT itself. The DAQC is controlled via an Algorithms for Control and Locking (ACL) server, a data computation pipeline developed by LAPP for interaction with instruments and actuators at Virgo. Input and output signals from the DAQC are observed using the Data Viewer software package developed for use at Virgo.

To lock the cavity, a ramp signal is first generated using the ACL interface. The amplitude, shape, and frequency of this signal are customizable; when attempting to achieve a lock, the signal is usually a 3  $V_{PP}$ , 0.01 Hz symmetric triangle wave, as shown in Fig 16. This signal is passed through the "Feedback from DAQC" input in Fig 18c. As the PZT moves the attached mirror, the length of the cavity increases and decreases, with resonance being achieved when the length is such that the IR pump beam constructively interferes with itself inside the cavity. Detector A outputs the DC photovoltage seen in Fig 17, with peaks occurring when the PZT has moved the mirror into a resonant position. The RF signal from Detector A is mixed with the EOM drive signal and passed through a low-pass filter to isolate the error signal, seen in Fig 19.

The ACL program establishes lock in two phases. During phase 1, the DAQC scans the cavity until the DC signal passes a given DC threshold value. At this point, the ramp

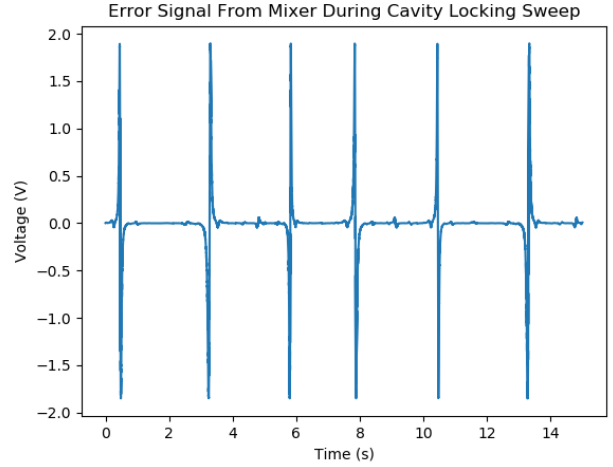


Fig. 19. Error signal extracted from Detector A's RF signal with PZT being driven by the ramp signal seen in Fig 16. The steep line in between extrema in each peak is the linear regime in which Eq 18 holds.

speed is slowed by a factor of 10 until the error signal passes a given AC threshold value. The program then enters phase 2, attempting to bring the error signal to zero - and keep it at zero - by making small corrections to the PZT's position. If at any point the error signal exceeds a "drop threshold" value, the program ceases attempts to maintain the lock and returns to sweeping the cavity until the DC signal again reaches the DC threshold. The process will then repeat, allowing for automatic lock re-acquisition. See the Appendix for an excerpt from the ACL code.

The ability of the system to achieve and maintain a lock is highly dependent upon the DC, AC, and drop threshold values, the scale factor of the error signal, and the gain of the DAQC's low-pass filter. The threshold values determine when to begin the locking process and when to abandon it. If the DC threshold is too low, the program might lock onto non-TEM00 peaks. If it is too high, the program might overshoot the peak before the ramp can be slowed. If the AC threshold is too low, the program might begin to use the error signal too close to a minimum or maximum, outside the signal's linear regime. If it is too high, the program might again overshoot the peak. The drop threshold must be high enough to prevent extreme oscillations of the PZT while low enough to allow the program to recover from sudden jolts. The scale factor and gain both determine how large the feedback signal will be relative to the error signal that generates it; too high a scale factor or low a gain and the program may overcorrect for noise and lose lock, too low a scale factor or high a gain and it may be unable to stop a drift away from resonance. These parameters thus had to be changed through a trial-and-error process until a stable, resilient lock was achieved, and had to be altered when IR pump power was changed.

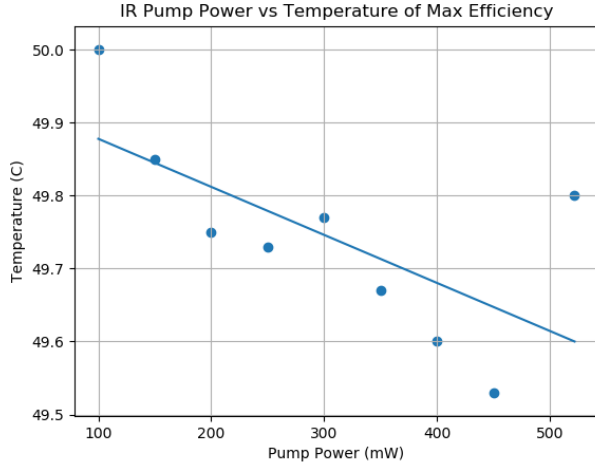


Fig. 20. Plot of temperature at which green light production from the SHG cavity was observed to be at a maximum vs IR pump power.

### E. SHG Efficiency Measurements

Before it is used in the ExSqueeze system, the SHG cavity must be characterized. The conversion efficiency and temperature of max efficiency as a function of pump power are needed for determining the operating points of the system. IR pump power and ambient temperature affect the temperature of the crystal and thus change the temperature controller setting at which maximum conversion efficiency is obtained; efficiency likewise varies with IR pump power.

Both these measurements were performed simultaneously. IR power entering the cavity (immediately preceding the 75 mm focal length lens in Fig 7) was increased from 100 mW to 522 mW, with Detector C being used to measure the beam's power. At each step, the SHG cavity was locked as described in the preceding subsection. The Covision Temperature Controller program (see Section III-B) was used to change the controller's setpoint until green output, as measured by Detector C at the position shown in Fig 7, was observed to be at a maximum. A plot of temperature of max efficiency vs IR pump power can be seen in Fig 20. Temperature generally declined with increasing pump power, as expected since additional power within the cavity generates heating beyond that provided by the controller. The variation was small, however, with all setpoints within a half degree across a range of input powers from 100 mW through 522 mW (about 20% of the maximum possible pump power). Changes in ambient temperature are a possible source of the deviation from linear behavior, as measurements were performed over several hours, with the point at 522 mW taken several hours after the other points. An additional source of error was fluctuations in output power due to lock instability, electrical interference, ambient light, and other noise sources, making it difficult to determine the true point of maximum green production.

Green output power was then recorded. Green power as a function of IR pump power is shown in Fig 21. The

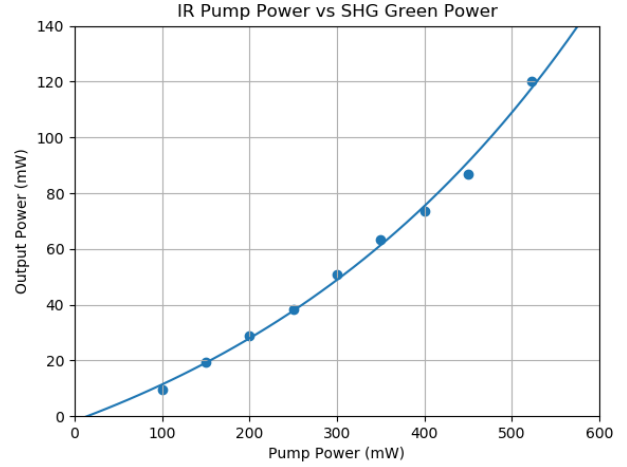


Fig. 21. Plot of output green power entering the MZI in Fig 7 as a function of IR pump power measured directly preceding the 75 mm focal length lens in front of the cavity, with best-fit function.

data appears to be somewhat linear; however, the exponential least-squares regression curve:

$$P_G(P_{IR}) = 49.4 * 1.002^{1.2P_{IR}} - 51.1 \quad (19)$$

Where  $P_G$  is output green power in milliwatts and  $P_{IR}$  is IR pump power in milliwatts, was found to provide a much better fit than first, second, third, or fourth order polynomials. The nonlinearity is likely due to the increase in conversion efficiency with increasing IR pump power. It is believed this function will provide a good approximation for green output power across the full range of accessible IR pump powers.

The conversion efficiency (the ratio between green output power and IR pump power) of the cavity as a function of IR pump power is shown in Fig 22. Efficiency increases in a relatively linear manner, with the equation of the linear fit being:

$$E(P) = 0.027P + 8.25 \quad (20)$$

Where  $P$  is the IR pump power in milliwatts and  $E(P)$  is the conversion efficiency as a percentage of IR pump power. A linear relationship between efficiency and pump power has previously been observed by other researchers at LKB working with a similar crystal and optical setup, so this result is not surprising. It is not presently known why the efficiency at 100 mW appears to be significantly lower than would be expected by a linear fit, nor why the efficiency at 522 mW appears to be unusually high. The linear relationship can hold only for a certain range of pump powers, and it is possible 100 mW and 522 mW fall outside of this range. It is also possible this deviation is simply due to error sources such as lock instability and vibrational and electrical noise.

### F. Detector A Calibration

An ultimate goal for the ExSqueeze project as a whole is remote control of all parts of the optical system. Operation without in-room intervention will significantly reduce noise

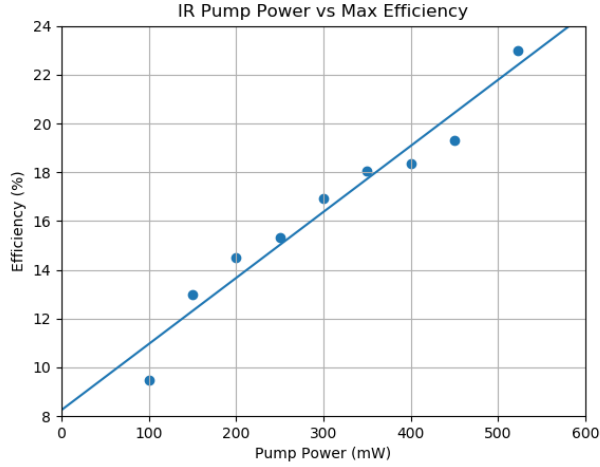


Fig. 22. Plot of conversion efficiency, the percent IR pump power converted by the SHG into green output power, as a function of IR pump power measured directly preceding the 75 mm focal length lens in front of the cavity in Fig 7

and is a requirement for implementation at Virgo. Throughout the measurements described in the previous sections, Detector C was manually inserted and removed from the optical path to measure IR pump power. This will not be possible in a remotely operated system. Instead, the signal from Detector A will be used to deduce the IR pump power entering the SHG cavity. To do this, the detector must first be calibrated. IR pump power immediately preceding the SHG cavity focusing lens (see Fig 7) was increased from 100 mW to 522 mW, as measured by Detector C. At each step, the cavity was locked and the average signal from Detector A during a two-second sweep was recorded. The results can be seen in Fig 23. Although response initially appears to be linear, a simulation performed by Dr. Chua, without accounting for optical losses or gains, indicated a quadratic relationship between IR pump power and power incident on Detector A. This is due to the observed increase in conversion efficiency with increasing IR pump power. Increased efficiency results in less IR light exiting the cavity as more is converted to green light, suggesting that while an increase in IR pump power would result in an increase in power seen by Detector A, the relationship would not be linear. The fit function used is:

$$V(P) = 0.443\sqrt{P + 553} - 10 \quad (21)$$

Where  $P$  is IR pump power in milliwatts and  $V(P)$  is the average signal generated by Detector A in volts. It is believed this function will provide a good approximation for Detector A's response across the full range of accessible IR pump powers.

#### IV. MACH-ZEHNDER INTERFEROMETER

The Mach-Zehnder Interferometer (MZI), seen in the highlighted region in Fig 7, is used to further stabilize green output power produced by the SHG prior to its injection

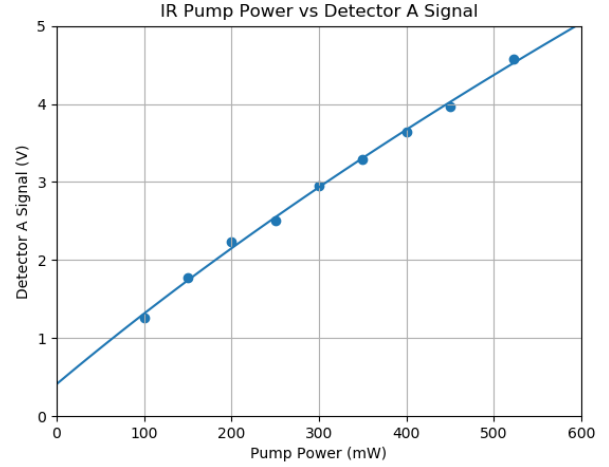


Fig. 23. Average voltage response of Detector A vs IR pump power measured immediately before the SHG cavity focusing lens, with a best-fit curve computed via least squares regression.

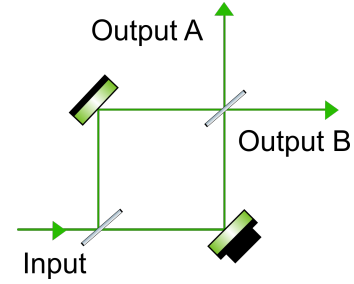


Fig. 24. Simplified optical diagram of a Mach-Zehnder Interferometer.

into the In-Vacuum Bench. The SHG cavity lock is naturally unstable due to seismic and acoustic vibrations in the optical bench, fluctuations in laser power, and electrical noise within the PDH control loop. Because of this, small fluctuations in green output power are unavoidable. To minimize them, the MZI is employed to divert fluctuations away from the In-Vacuum Bench.

#### A. Mach-Zehnder Interferometer Theory of Operation

Fig 24 presents a simplified optical schematic of a MZI. A laser beam, in this case green light from the SHG, is sent through a 70% reflection, 30% transmission beamsplitter. The two resulting beams each reflect off a mirror and converge at a second 70:30 beamsplitter, where they are made to interfere and produce two output beams. If the the path traveled by each beam is the same (or if the path length difference is an integer multiple of the wavelength), the summed light field will be maximized at output A and minimized at output B; all power will be in output A. If the path length difference is exactly one half of a wavelength, the opposite will be true; the field at output A will be minimized, and the field at output B will be maximized, diverting all power towards output B. Changing the position of one of the mirrors, then, allows for precise control of the ratio of power in output A vs output B. In the ExSqueeze system, the MZI

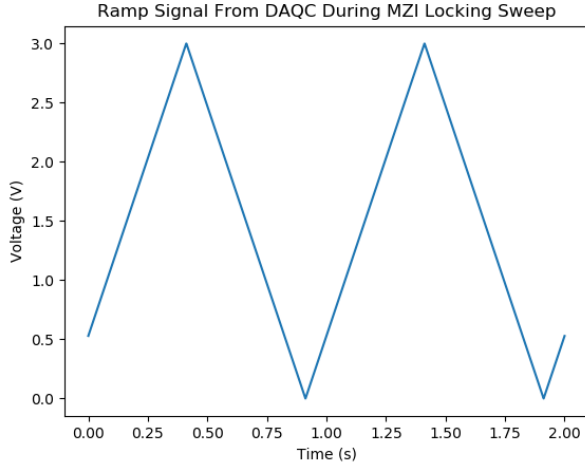


Fig. 25. Signal sent by DAQC to MZI PZT during locking sweep.

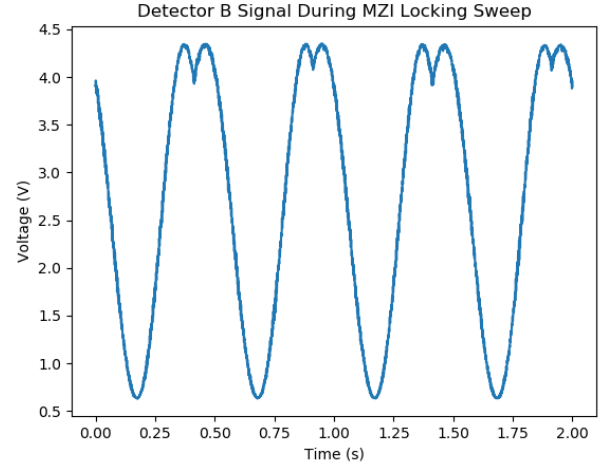


Fig. 26. Signal from Detector B with PZT being driven by the ramp signal seen in Fig 25.

is locked such that the output going towards the In-Vacuum Bench is kept at a constant value while the output going towards the beam dump contains the residual fluctuations, the mirror attached to the PZT being adjusted to ensure this is the case.

### B. MZI Locking

The control loop for the MZI is contained within the DAQC and managed through a modified ACL script similar to the control scheme used for the SHG cavity (see Section III-D, and the Appendix for an excerpt of this code). However, the PDH technique is not used.

Locking is again carried out in two phases. In phase 1, the PZT is driven by a  $3 V_{PP}$ , 1 Hz symmetric triangle wave as shown in Fig 25 from the DAQC, passed through the second output of the x50 voltage amplifier used for the SHG cavity. This produces an interference fringe pattern on Detector B; the signal produced by Detector B in response to this can be seen in Fig 26. This signal is sent directly to the DAQC, and an error signal is generated by subtracting a constant user-defined locking voltage from the photovoltage (Fig 27). The ramp is slowed by a factor of ten once the signal passes a user-defined threshold value but continues until the error signal passes another user-defined threshold value, at which point the system enters phase 2. Small adjustments are made to the PZT as the feedback loop attempts to bring the error signal to zero, thereby locking the voltage - and the optical power within the In-Vacuum output corresponding to this voltage - at the user-defined level. Lock is not made at maximum output as this would provide too little flexibility to the system when attempting to correct for fluctuations; it would not be able to shift more power to the In-Vacuum output when SHG output declines as all light would already be in this output. The ideal lock position is thus slightly off of an interference peak.

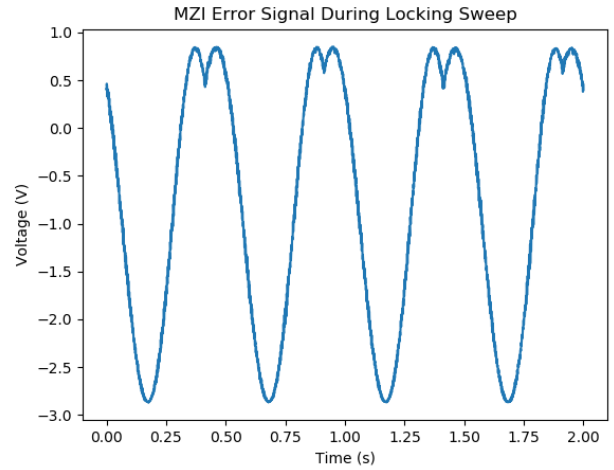


Fig. 27. Error signal generated from Detector B signal seen in Fig 26 with a locking voltage of 3.5 V.

### C. Detector B Calibration

The purpose of the MZI is to precisely control the amount of green light entering the In-Vacuum Bench. Consequently, a way of measuring this power is needed. During initial testing, Detector C was placed in the optical path to detect green light power. However, for the reasons described in Section III-F, it is desirable to use Detector B instead. This requires the relationship between Detector B's signal and the power of green light entering the In-Vacuum Bench to be determined. To do this, Detector C was placed at the In-Vacuum Bench output seen in Fig 7. The lower arm of the MZI - with the non-PZT mirror - was blocked, and 350 mW of IR pump laser was sent into the SHG cavity. The cavity was locked, producing approximately 64 mW of green light as measured immediately preceding the MZI. Reflectance of the MZI beamsplitters is polarization-dependent, and was observed to be approximately 80% during the experiment.

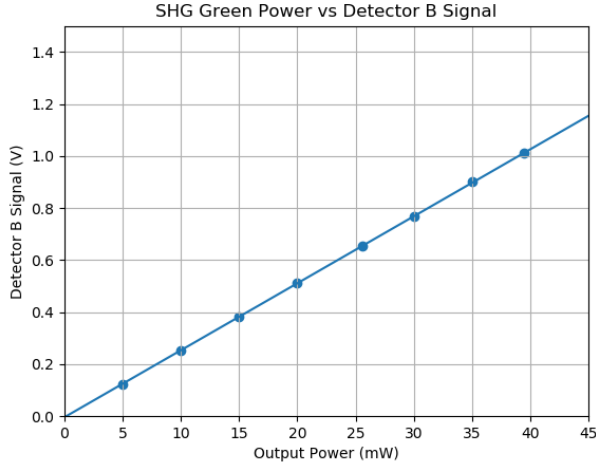


Fig. 28. Average voltage response of Detector B vs green power measured at the In-Vacuum Bench output, with a best-fit linear regression line.

Thus, about 41 mW of green light exited the half-MZI, without factoring in losses from other sources. The half-wave plate preceding the polarized beamsplitter after the MZI was rotated to increase the light incident on Detector C from 5 mW to 39.5 mW, and the average signal generated by Detector B over a two-second sweep was recorded. The results can be seen in Fig 28. Response is highly linear, as expected based on information in the detector’s datasheet. An increase in green power transmitted to the vacuum bench results in a proportional increase in green power sent to the detector, with a scale factor of approximately 0.01 due to the 1% beam sampler used. The following function for Detector B’s voltage response was derived through liner regression:

$$V(P) = 0.0257P - 0.00375 \quad (22)$$

where  $P$  is the power at the In-Vacuum output in milliwatts and  $V(P)$  is the average signal generated by Detector B in volts. It is believed this function will provide a good approximation for Detector B’s response across the entire range of output powers generated by the system.

## V. CONCLUSION

We successfully constructed and characterized a second harmonic generator and Mach-Zehnder interferometer. The ability to achieve and maintain a stable lock in both systems is essential for the production of a stable squeezed vacuum state by the rest of the ExSqueeze setup, which is in turn necessary for the generation of frequency-dependent squeezed light. Characterization of the efficiency and temperature response of the SHG cavity will help determine expected output green power for a given IR pump power, useful information when determining the operating points of the system as a whole. Finally, in-situ calibration of the photodetectors and creation of ACL and Python control programs are important steps towards the creation of an entirely remote interface for CALVA. The SHG-MZI segment of the

ExSqueeze setup is now ready for integration with the In-Vacuum Bench and rotation cavity.

## ACKNOWLEDGEMENT

I would like to thank everyone on the Optomechanics and Quantum Measurement team at Laboratoire Kastler Brossel and the Laboratoire de l’Accélérateur Linéaire for welcoming me into their lab and helping me throughout this project. I would especially like to thank Dr. Sheon Chua, Dr. Pierre-François Cohadon, and Michaël Croquette for their guidance and support during my time in Paris. I would also like to thank Dr. Guido Mueller, Dr. Bernard Whiting, and Andrew Miller for all their hard work arranging for my stay in Paris and organizing the International REU program, as well as the University of Florida and National Science Foundation for providing me with this amazing experience.

## REFERENCES

- [1] B P Abbot et al., “Observation of Gravitational Waves from a Binary Black Hole Merger,” *Physical Review Letters* vol 116 no 6 (2016). doi: 10.1103/PhysRevLett.116.061102
- [2] S S Y Chua, B J J Slagmolen, D A Shaddock and D E McClelland, “Quantum squeezed light in gravitationalwave detectors,” *Classical and Quantum Gravity* vol 31 no 18 (2014). doi: 10.1088/0264-9381/31/18/183001
- [3] M Houe and P D Townsend, “An introduction to methods of periodic poling for second-harmonic generation,” *Journal of Physics D: Applied Physics* vol 28 no 9 (1995). doi: 10.1088/0022-3727/28/9/001
- [4] R. W. Boyd, *Nonlinear Optics* 2nd edn, Elsevier Science USA (2003).
- [5] P F Cohadon et al., “Experimental Squeezing for Optomechanics,” Proposal to the Agence Nationale de la Recherche
- [6] E Black, “An introduction to Pound-Drever-Hall laser frequency stabilization,” *American Journal of Physics* vol 69 no 79 (2001). doi: 10.1119/1.1286663
- [7] C. Bond, D. Brown, A. Freise, and K. Strain, “Interferometer techniques for gravitational-wave detection,” *Living Reviews in Relativity* vol 13 no 1 (2010). doi: 10.12942/lrr-2010-1
- [8] S Chelkowski et al., “Experimental characterization of frequency-dependent squeezed light,” *Physical Review A* vol 71 no 1 (2005). doi: 10.1103/PhysRevA.71.013806



## Appendix

### Sample of OC2 Temperature Controller Python program:

```
#Class defining the temperature controller
class temp_cont:
    #Initialization method establishes communications with the controller and sends it the
    #last-known control and setpoint parameters
    def __init__(self, address, baud):
        #Instantiate the visa resource manager class
        rm=visa.ResourceManager()
        #Define the "i" attribute to be the visa instrument object
        self.i=rm.get_instrument(address)
        #Set the baud rate
        self.i.baud_rate=baud
        #Get config file. The config file will follow the module packet wherever it goes.
        #__file__ retrieves the name and directory of this program. The name is then removed,
        #leaving only the directory, to which is added the name of the config file. This
        #permits easy operation when the program is transferred to a new device
        self.config_dir=__file__.replace(os.path.split(__file__)[1], '')+'config.json'
        #Read the config file
        config=open(self.config_dir, 'r')
        #Load the config file. The file is a 2x2 list; one list goes to each hidden
        #attribute here
        self._control_params, self._setpoint_params=json.load(config)
        #Close the config file
        config.close()
        #Reset the control and setpoint parameters to the values indicated in the config file.
        #Due to the inability to query the controller for this information, a constant
        #record of these parameters will be kept in the config file. Since some values
        #reset upon controller power-down and some do not, all will be reset to the config
        #values upon initialization
        self.change_control_params(self._control_params)
        sleep(0.1)
        self.change_setpoint_params(self._setpoint_params)

    #Method to finalize a command string by adding the checksum and start-of-heading
    #characters
    def checksum_writer(self, string):
        #Start a list of ascii values with 1, the start-of-heading character, at index
        #position 0.
        ascii_array=[1]
        #Run through each character in the string
        for char in string:
            #Convert each to it's ascii value
            ascii_array.append(ord(char))
        #Return the final command string, with the start-of-heading character, the string,
        #and the checksum, equal to the hexadecimal value of the sum of the ascii values
        #mod 256. Note that Python adds a '0x' prefix to hex values, hence the omission
        #of the first two characters of the checksum, and all letters must additionally be
        #capitalized because that's how the controller likes it
        return chr(1)+string+str(hex(sum(ascii_array)%256))[2:].upper()

    #Method to convert sent parameter information to the proper format: all strings, with the
```

```

#correct number of digits
def formatter(self, lis, decs):
    #Declare a list to house the final versions of the parameters
    fin_lis=list()
    #Run through each element in the list
    for j in range(len(lis)):
        #Format the parameter value given in lis to the number of decimal places given in
        #the format code in decs
        fin_lis.append(decs[j]%float(lis[j]))
    #Return a list of specific-length strings
    return fin_lis

#Method to change the control (feedback loop) parameters of the controller.
def change_control_params(self, new_control_params):
    #Parameter values may be sent as floats, integers, or strings. They must be turned into
    #strings with the correct number of digits of precision. This method does that.
    new_control_params=self.formatter(new_control_params, ["%i", "%.3f", "%.3f", "%.3f", +
        + "%.3f", "%.3f"])
    #Assign the control parameters attribute to the new values
    self._control_params=new_control_params
    #Arrange the list elements in the proper command format
    cmdstr=self._control_params[0]+';'+self._control_params[1]+';'+self._control_params[2]+
        '+';'+self._control_params[3]+';'+self._control_params[4]+';'+self._control_params[5]+
        '+';'+ '1'+';'
    #Add the 'a' command code, which signifies a control parameter alteration command, as
    #well as the length of the base command string
    cmd_init='a'+str(len(cmdstr))+cmdstr
    #Send the base command string to the checksum_writer for finalization
    cmd=self.checksum_writer(cmd_init)
    #Write the finalized command string to the controller
    self.i.write(cmd)
    #Update the config file
    config=open(self.config_dir, 'w')
    json.dump([self._control_params,self._setpoint_params], config)
    config.close()
    return

#Method to change the temperature setpoint parameters of the controller.
def change_setpoint_params(self, new_setpoint_params):
    #Parameter values may be sent as floats, integers, or strings. They must be turned into
    #strings with the correct number of digits of precision. This method does that.
    new_setpoint_params=self.formatter(new_setpoint_params, [ "%.3f", "%.3f", "%.3f", "%i", +
        + "%.2f", "%.2f"])
    #Assign the setpoint parameters attribute to the new values
    self._setpoint_params=new_setpoint_params
    #Arrange the list elements in the proper command format
    cmdstr='1;'+self._setpoint_params[0]+';'+self._setpoint_params[1]+';'+
        +self._setpoint_params[2]+';'+self._setpoint_params[3]+';'+self._setpoint_params[4]+
        '+';'+self._setpoint_params[5]+';'
    #Add the 'i' command code, which signifies a setpoint parameter alteration command, as
    #well as the length of the base command string
    cmd_init='i'+str(len(cmdstr))+cmdstr
    #Send the base command string to the checksum_writer for finalization
    cmd=self.checksum_writer(cmd_init)

```

## Sample of Python Code for Lens Mode Matching:

```
#Function finding the location and size of the output waist given lens positions
def loc_from_lens(plc1, plc2, w1, wvlen, f1, f2, accuracy):
    #A bunch of intermediate values
    zo1=pi*w1**2/wvlen
    r1_at_1=plc1*(1+(zo1/plc1)**2)
    r2_at_1=1/(1/r1_at_1-1/f1)
    w1_at_1=w1*sqrt(1+(plc1/zo1)**2)
    w2=w1_at_1/sqrt(1+(pi*w1_at_1**2/(wvlen*r2_at_1))**2)
    w2_at_1=w1_at_1
    waist2_loc=-r2_at_1/(1+(wvlen*r2_at_1/(pi*w1_at_1**2))**2)
    zo2=pi*w2**2/wvlen
    w2_at_2=w2*sqrt(1+(abs(waist2_loc-plc2)/zo2)**2)
    r2_at_2=abs(waist2_loc-plc2)*(1+(zo2/abs(waist2_loc-plc2))**2)
    r3_at_2=1/(1/r2_at_2-1/f2)
    w3=w2_at_2/sqrt(1+(pi*w2_at_2**2/(wvlen*r3_at_2))**2)
    zo3=pi*w3**2/wvlen
    w3_at_2=w2_at_2
    loc=abs(r3_at_2/(1+(wvlen*r3_at_2/(pi*w2_at_2**2))**2))
    #Round the answers to the desired precision
    w3=rounder(w3, accuracy)
    loc=rounder(loc, accuracy)
    return w3, loc

#Function finding the lens positions necessary to produce a desired waist size at the desired
#location.
def lens_from_loc_master(d, f1, f2, zo1, zo3, Wo1, Wo3, wvlen, accuracy):
    #Intermediate values
    #Radius at the left of the first lens, which is the same at right as well
    def W11_f(d1):
        return Wo1*sqrt(1+(d1/zo1)**2)
    #Radius of curvature at the left of the first lens
    def R11_f(d1):
        return d1*(1+(zo1/d1)**2)
    #Radius of curvature at the the right of the first lens (derived via the thin lens
    #approximation)
    def R21_f(d1):
        R11=R11_f(d1)
        return (f1*R11)/(f1-R11)
    #Waist size of inter-lens beam
    def Wo2_f(d1):
        R21=R21_f(d1)
        W11=W11_f(d1)
        return W11/sqrt(1+(pi*W11**2/(wvlen*R21))**2)
    #Location of waist of inter-lens beam. If it is negative, the waist does not physically
    #exist, but this doesn't matter for further calculations
    def k_f(d1):
        R21=R21_f(d1)
        W11=W11_f(d1)
        return -R21/(1+(wvlen*R21/(pi*W11**2))**2)
    #Space between the lenses
    def d2_f(d1):
        R21=R21_f(d1)
```

```

W11=W11_f(d1)
k=k_f(d1)
Wo2=Wo2_f(d1)
zo2=(pi*Wo2**2)/wvlen
#There are two possibilities since the d2 function is quadratic.
d2_p=(-(2*d-2*d1-2*k*Wo3**2/(Wo2**2))+sqrt((2*d-2*d1-2*k*Wo3**2/(Wo2**2))**2+
+ (-4)*((Wo3**2)/(Wo2**2)-1)*((zo2**2*Wo3**2)/(Wo2**2)+(k**2*Wo3**2)/(Wo2**2)+
+ (-zo3)**2-d**2-d1**2+2*d*d1)))/(2*((Wo3**2)/(Wo2**2)-1))
d2_n=(-(2*d-2*d1-2*k*Wo3**2/(Wo2**2))-sqrt((2*d-2*d1-2*k*Wo3**2/(Wo2**2))**2+
+ (-4)*((Wo3**2)/(Wo2**2)-1)*((zo2**2*Wo3**2)/(Wo2**2)+(k**2*Wo3**2)/(Wo2**2)+
+ (-zo3)**2-d**2-d1**2+2*d*d1)))/(2*((Wo3**2)/(Wo2**2)-1))
#The true solution should give a physically realizable output waist location, e.g. positive
if (d-d1-d2_p)>=0:
    return d2_p
else:
    return d2_n

```

### Sample of ACL Code for SHG Cavity and MZI locking:

```
##----- Acl server parameters
define LOOP_FREQ 10000
define DAC1955_FREQ 100000

# SMS prefix - CmTimeout - rtCpuId - load delay(s) - - DAQ frame freq(Hz) - memory flag
ACL_MAIN_LX "EXS_" 1 0 0.0

# Loop Frequency(Hz) - loop Delay(s) - minimal elapsed time - stat flag

ACL_TIMING LOOP_FREQ 0 0 0

ACL_INFO_OPTION 20

# Enable SMS facility
ACL_SMS ""

ACL_FILTER_DEFAULT_MAX_ORDER 2

ACL_SUFFIX_NAME "inphase" "_I"
ACL_SUFFIX_NAME "quadrature" "_Q"

ACL_CONST_CH null_100kHz "V" 0 DAC1955_FREQ 0

## Extract clock signal
# nameOut - unit - rampTime - samplingFreq - nameIn - offset - gain - filterName
ACL_ADC_CH clock_12MHz_ACp "V" 1 LOOP_FREQ clock_12MHz_ACp 0 1 "NONE"
ACL_ADC_CH clock_12MHz_ACq "V" 1 LOOP_FREQ clock_12MHz_ACq 0 1 "NONE"

ACL_OP_CH clock_12MHz_raw "" "mag|phi" clock_12MHz_ACp clock_12MHz_ACq
ACL_OP_CH clock_12MHz_raw_dFreq "" "derivative" clock_12MHz_raw_phi
ACL_INFO clock_12MHz_raw_mag clock_12MHz_raw_dFreq

ACL_DAQ "" "" clock_12MHz_raw_mag clock_12MHz_raw_phi clock_12MHz_raw_dFreq

## Extract SHG
ACL_ADC_CH SHG_12MHz_ACp "V" 1 LOOP_FREQ SHG_12MHz_ACp 0 1 "NONE"
ACL_ADC_CH SHG_12MHz_ACq "V" 1 LOOP_FREQ SHG_12MHz_ACq 0 1 "NONE"

ACL_OP_CH SHG_12MHz_raw "" "mag|phi" SHG_12MHz_ACp SHG_12MHz_ACq
ACL_OP_CH SHG_12MHz_raw_dFreq "" "derivative" SHG_12MHz_raw_phi
ACL_INFO SHG_12MHz_raw_mag SHG_12MHz_raw_dFreq

ACL_DAQ "" "" SHG_12MHz_raw_mag SHG_12MHz_raw_phi SHG_12MHz_raw_dFreq

ACL_CONST_CH SHG_12MHz_phi0 "rad" 0 LOOP_FREQ -0.0 # -5PI/24
ACL_SUM_CH SHG_12MHz_phiCorr "" 0 1 SHG_12MHz_phi0 1 clock_12MHz_raw_phi ;
#ACL_ROTATE_LINE_PHI_CH SHG_12MHz SHG_12MHz_ACp SHG_12MHz_ACq "" SHG_12MHz_phiCorr "none"

ACL_ROTATE_LINE_PHI_CH SHG_12MHz_init SHG_12MHz_ACp SHG_12MHz_ACq "" SHG_12MHz_phiCorr "none"
ACL_CONST_CH SCALE_CH au 0 LOOP_FREQ 3
ACL_OP_CH SHG_12MHz_I "" SHG_12MHz_init_I * SCALE_CH
ACL_OP_CH SHG_12MHz_Q "" SHG_12MHz_init_Q * SCALE_CH
```